nuclear fusion
IAEA

PAPER • OPEN ACCESS

Challenges and approaches to interpretive modeling of boundary plasma and neutral transport in a closed, pumped divertor

To cite this article: R.S. Wilcox *et al* 2026 *Nucl. Fusion* **66** 016023

OPEN ACCESS
IOP Publishing | International Atomic Energy Agency
Nuclear Fusion
Nucl. Fusion **66** (2026) 016023 (18pp)
https://doi.org/10.1088/1741-4326/ae1bb9

Challenges and approaches to interpretive modeling of boundary plasma and neutral transport in a closed, pumped divertor

R.S. Wilcox[1,*], M.W. Shafer[1], J.D. Lore[1], J.M. Canik[2], S.R. Haskey[3], C.J. Lasnier[4], A.L. Moser[5], T.H. Osborne[5] and H.Q. Wang[5]

[1] Oak Ridge National Laboratory, Oak Ridge, TN 37831, United States of America
[2] Type One Energy Group, Knoxville, TN 37931, United States of America
[3] Princeton Plasma Physics Laboratory, Princeton, NJ 08540, United States of America
[4] Lawrence Livermore National Laboratory, Livermore, CA 94550, United States of America
[5] General Atomics, San Diego, CA 92186, United States of America

E-mail: wilcoxrs@ornl.gov

Received 13 February 2025, revised 6 October 2025
Accepted for publication 5 November 2025
Published 17 November 2025

Abstract

An experimental discharge from the DIII-D tokamak is modeled using the SOLPS-ITER code suite and compared against measurements in the pumped and relatively closed upper divertor. Uncertainties of boundary plasma simulations are identified by attempting to match code inputs to experimental conditions, including iteratively solving transport coefficients to match upstream experimental profiles using varying quantities of core particle flux, different pumping models, and various assumptions of ion thermal transport. Simulated boundary conditions for particle injection at the core interface are shown to be relevant to the plasma solution at the divertor targets, even if upstream transport is modified so that plasma profiles are comparatively similar, although seperatrix density is not held constant. When upstream plasma profiles are matched to experimental measurements by varying diffusive transport coefficients, using either poloidally symmetric or ballooning structure, the model finds a majority of injected energy being transported radially off the computational domain, in conflict with experimental radiated power measurements and heat flux measurements at the divertor target. Imposing a maximum thermal diffusivity or radially shifting the experimental separatrix location of the fitted profiles to increase power conducted to the targets by increasing the upstream electron temperature does not significantly modify this result. Including a thermalizing plenum volume in the simulation domain is shown to maintain the experimental volumetric pumping rate without knowing the neutral energy distribution incident on the pump duct *a priori*. By modifying transport parameters to match different assumptions for ion temperature, downstream neutral pressure changes by more than a factor of two, suggesting that attention to ion thermal transport may be a

* Author to whom any correspondence should be addressed.

critical parameter for simulations to accurately resolve recycling and neutral transport, particularly in a closed divertor geometry. In addition to quantifying various modeling uncertainties, this work motivates both further experimental study and modeling improvements to improve predictive capabilities.

Keywords: tokamaks, divertor, modeling

(Some figures may appear in colour only in the online journal)

1. Introduction

In recent decades, understanding of plasma confinement on closed flux magnetic surfaces in tokamaks has begun to approach the point of a predictive model that can be used to extrapolate to next-step devices [1, 2]. These core models, however, require a boundary condition to be defined at somewhere the plasma edge. A similarly predictive understanding of the boundary plasma and exhaust system is arguably not yet available, and even the most advanced models of the core plasma system require boundary conditions to be provided from field lines with parallel connections to material surfaces, leaving this as a critical gap in whole device plasma modeling. Integrated plasma fluid and neutral particle modeling suites have been and continue to be developed for modeling the plasma boundary [3–7], but detailed validation efforts demonstrate that, although reasonable agreement can be found between the codes in many areas, capture of all critical physics seemingly remains out of reach, and none of the models[6] to date can be expected to be predictive at reactor scales [8–10].

Despite these challenges, boundary plasma simulation codes are critical for predicting plasma and neutral conditions near the divertor targets and main chamber walls when designing new devices, or new divertors for existing devices [8, 11–20]. They are often used to provide guidance for engineering tolerances of particle and particle exhaust loads, to plan for diagnostic needs, or to provide additional information about plasma conditions in existing devices with relatively sparse diagnostics. In the future they will be needed to determine erosion rates for plasma facing materials in both the divertor and the main chamber. Validation of computational models using existing experiments is therefore critical to improving their fidelity and increasing confidence in their predictive capabilities. Part of this process is learning which inputs to the simulations are most important to accurately reproduce experimental data. Another is identifying places where the model requires fundamental improvement.

An effort has been made through the work presented here to match model inputs as closely as possible to experimental measurements in order to quantify sensitivities to these parameters. For this study, a relatively closed divertor geometry was used as a step towards a potentially more reactor-relevant solution to the tokamak core-edge integration problem [21–23], and to examine the challenges that this geometry presents when using existing boundary plasma modeling tools. One of the limitations of modeling these closed geometries with SOLPS-ITER is that the plasma simulation mesh does not extend to the first wall. An extended grid version of the code has been developed for SOLPS [24, 25] as well as similar boundary codes like SolEdge [26, 27]. While this important work may remove the unphysical boundary condition on the SOLPS fluid equations, many of the challenges discussed here that focus on the radial locations close to the separatrix are likely to remain for some time. More physics-based cross-field transport models are also emerging [28], but developing these models into something that encapsulates all relevant instabilities and transport processes will likely take a number of years, especially since even these emerging techniques still lack a first-principles physics model and rely on fitting to observed conditions in current machines.

The remainder of the paper is structured as follows: section 2 presents the setup of the SOLPS-ITER simulations. Section 3 then explains the procedure and results for matching upstream plasma profiles in the simulations with experimental measurements, and section 4 analyzes the heat flux that is often transported off the computational domain in the process of this radial transport fitting. Section 5 discusses the simulation results of including a modeled pumping plenum volume, as well as changing assumptions for ion thermal transport. A discussion of the implications of these results is given in section 6, and finally, section 7 presents a summary and conclusions.

2. Setup for interpretive modeling

The starting point for the experimental tokamak discharge modeled here is DIII-D shot 180 344 at 2300 ms. This shot was run with the active X-point in the relatively closed upper divertor, where the upper, outer cryopump was turned on (cooled to liquid helium temperature). The other two cryopumps in DIII-D, in the upper, inner dome and lower, outer baffle, were not actively pumping. Toroidal magnetic field B_T in the stationary part of the discharge was 2.0 T and plasma current I_P was 1.3 MA in the same direction as B_T, resulting in an edge safety

[6] Notice: This manuscript has been authored by UT-Battelle, LLC, under contract DE-AC05-00OR22725 with the US Department of Energy (DOE). The US government retains and the publisher, by accepting the article for publication, acknowledges that the US government retains a nonexclusive, paid-up, irrevocable, worldwide license to publish or reproduce the published form of this manuscript, or allow others to do so, for US government purposes. DOE will provide public access to these results of federally sponsored research in accordance with the DOE Public Access Plan (https://www.energy.gov/doe-public-access-plan).

factor q_{95} between 3.9 and 4.0 and ion $B \times \nabla B$ drift directed up, towards the active divertor (i.e. favorable for H-mode access).

Injected power from neutral beams was 6.15 MW during the stationary phase of this shot, and no electron cyclotron heating was used. The time slice around 2300 ms was selected because the plasma had evolved into a quasi-stationary ELMing H-mode with stable macroscopic plasma parameters such as density and stored energy. No gas puffing was used in the experiment around this time, so that the plasma was fueled entirely by neutral beam particles and recycling flux.

Boundary plasma simulations presented here were performed using SOLPS-ITER, version 3.0.8 [3, 29]. The 2D plasma and extended neutral grids used for these simulations are shown in figure 1, which includes a simplified representation of the upper outer plenum volume containing the active cryopump. The effect of including or neglecting this plenum volume in the computational domain will be presented in section 5.1. The neutral model employed fully kinetic Monte Carlo neutrals via EIRENE, and neutral–neutral collisions between deuterium atoms and molecules were included in the reaction set. Transport coefficients were iteratively modified to match upstream experimental measurements in the array of cells labeled in red in figure 1, at the location of the pedestal Thomson scattering diagnostic, as will be discussed in section 3. Carbon impurities were included in the simulations, sourced via physical sputtering at the target in addition to 2% chemical sputtering from deuterium particles incident on carbon tiles. No sputtering occurs at the grid boundaries where there are not material surfaces. This level of sputtering resulted in the fully stripped carbon ion density matching the quantity measured by charge exchange recombination spectroscopy (CER) upstream near the outboard midplane (OMP) in the vicinity of the separatrix within the measurement uncertainty, such that one might expect the model to approximately reproduce the edge carbon radiation when electron temperature and density are also matched. Measured carbon densities inside the pedestal top (ψ_n <0.97) were larger in the experiment than in the simulation by a factor of 2–3. Because the study here focused on the plasma exhaust rather than examining the pedestal or core, and because larger challenges to matching the experimental power balance were encountered that will be discussed later in section 3, no effort was made to modify impurity transport coefficients separately from the main ions to match the core impurity density profile further inside the separatrix.

Due to the computational expense of cross-field plasma drifts, these effects were not included in the simulations here. The ion $B \times \nabla B$ drift was directed upward for these experiments, into the active divertor. It is therefore expected that the effect of drifts would be to transport particles from the outer divertor to the inner divertor, somewhat rarefying the density and increasing the temperature in the outer target region [30].

To accommodate the relatively closed geometry of the upper divertor in DIII-D while including the pumping plenum in the EIRENE domain for more realistic neutral particle

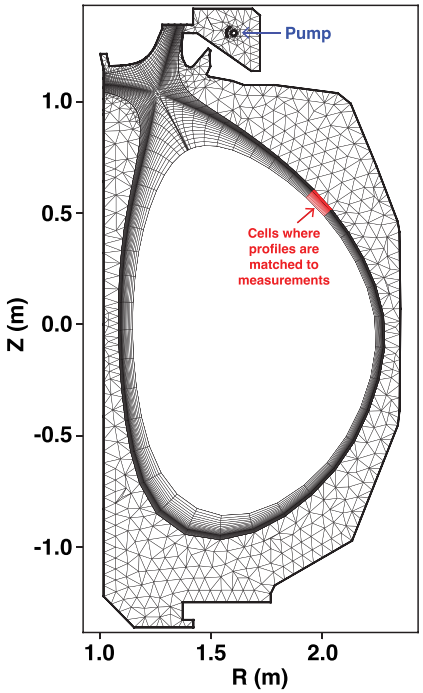

Figure 1. Computational grid for both plasma and neutral species using SOLPS-ITER.

simulations, the radial extent of the plasma grid is truncated before the pump duct opening, thus including 6.7 mm of magnetic flux at the outer midplane. This encompasses more than 2 heat flux widths at the entrances to the divertor in the simulation, but may still lead to some known modeling inconsistencies, including local recycling applied to ions escaping the domain [31] and a physically large neutral penetration in locations where sparse far scrape-off layer (SOL) plasmas that would nominally ionize neutrals are now replaced with near-vacuum conditions [24, 32]. The H-mode heat flux width would be expected to be ∼2 mm at the OMP based on multi-machine scalings [33], which is similar to what is found in this series of simulations employing the profile matching technique. Further discussion of fluxes escaping the plasma domain is included in section 3. For speedup, the `eirene_mod` input was set to 5 (EIRENE was only run once for every five time steps of B2), while `b2mndt_nstg2` was set to 1 (1 internal iteration of B2 per time step). Time steps for the final cases presented here were no larger than 1×10^{-5} s.

2.1. Particle and energy sources and sinks

For the purposes of interpretive modeling and code validation, model inputs are selected carefully to be as representative as possible of the true physical system at the time of interest during the plasma discharge. Power injected at the simulation's core grid boundary was taken as 80% of the experimentally injected neutral beam power, evenly divided between the electrons and ions (2.46 MW each). This fraction was selected to

account for the rate of change of the plasma-stored diamagnetic energy, dW/dt, in the latter half of the ELM cycle when the profile data was extracted. This is also consistent with the previously reported observation that roughly 20% of injected power in DIII-D is ejected during ELMs across a broad range of injected powers in neutral beam-heated H-mode plasmas [34].

The ion particle flux injected at the core grid boundary was initially prescribed to match the time-averaged particle source of the neutral beams at the relevant time period, 7.14×10^{20} deuterium atoms per second. As will be shown later, these quantities are modified in some cases to match the experimental particle removal rate measured by a calibrated neutral pressure gauge, which was approximately three times the value of injected particles at the time of interest, likely due to the desorption of residual gas that had been retained in tiles during previous discharges. Because most neutralized particles can remain in the vessel and be re-ionized following their ejection from the core by an ELM, unlike the thermal energy which leaves the plasma-neutral system quickly, no modification to the modeled steady-state particle injection rate is made to account for the transient uptake of particles in the core between ELMs in the same way that injected energy was modified.

For these simulations, the fraction of neutral particles incident on a modeled pumping surface that are removed from the computational system (f_{pumped}) is selected as a code input according to the equation

$$f_{\text{pumped}} = \frac{4S_{\text{pump}}}{\bar{v}A_{\text{pump}}}, \tag{1}$$

where S_{pump} is the desired volumetric pumping rate, $\bar{v}$ is the average velocity of particles incident on the surface, and A_{pump} is the surface area of the pumping surface in the model. The particle reflection coefficient set in the EIRENE input file is then one minus f_{pumped}. For the work presented here, $\bar{v}$ is assumed to be the velocity of molecular deuterium thermalized to a Maxwellian distribution centered at the wall temperature away from the target (300 K). This assumption is valid in the case here where the pumping surfaces are all deep in the plenum behind a thermalizing plate, so that there is no line of sight between energetic neutrals and the pump without first bouncing off a wall surface. Implications of this assumption being violated will be discussed in section 5.1. S_{pump} is then taken to be 40 m^3 s^{-1} for the upper, outer pump of DIII-D based on previously calibrated measurements [35].

All main chamber wall surfaces here are set to recycle 100% of incident particles. This is consistent with DIII-D experiments that demonstrated that the carbon walls, once saturated, have an approximate global retention rate of zero, within experimental uncertainties, during the later stationary phases of pumped H-mode discharges [36]. Main chamber surfaces were set to reflect neutral particles with a Maxwellian energy distribution centered around 0.026 eV (∼300 K), while target surfaces were set to 0.043 eV (∼500 K) as a crude estimate of hotter tiles at the target. Thermocouple or infrared camera measurements could be used to set poloidally varying wall temperatures in future work to test its impact on modeled neutral ionization profiles. Neutral particles reaching the core boundary were re-ionized and added to the user-defined core particle flux boundary condition to maintain particle conservation in the simulation.

Numerical convergence is often more easily achieved by including some finite absorption of particles by main chamber surfaces, so this can be useful in early iterations of SOLPS calculations, but even small values of fractional particle absorption can lead to volumetric pumping that significantly impacts global particle balance due to the large surface area of the main chamber. For example, from equation (1), pumping 1% of the incident particles on every surface in DIII-D equates to a volumetric pumping rate of approximately 240 m^3 s^{-1} for the 76 m^2 of surface area on the walls, assuming the average particle velocity is D_2 at 300 K. This is roughly 6 times the volumetric pumping rate of the upper outer pump.

3. Upstream profile matching

In an attempt to match the critical simulation quantities with the experiment, the upstream radial profiles of plasma temperature and density in SOLPS-ITER can be modified via user-provided diffusive transport coefficients [37]. Experimental measurements of electron temperature (T_e) and density (n_e) from Thomson scattering are compared here against the modeled values in a radial array of grid cells in the poloidal position closest to the Thomson scattering measurement, labeled in red in figure 1. Comparisons of simulated ion temperature with measurements are presented later in section 5.2, along with a discussion of the physics implications of matching T_i independent of T_e.

3.1. Iterative solving of transport coefficients

In order to establish SOLPS plasma profiles that match experimental measurements, the diffusive transport coefficients are updated iteratively until the converged SOLPS solution reaches acceptable agreement with experimental profiles, within measurement uncertainty if possible. At each step, the diffusive coefficients for radial particle (D) and thermal transport for electrons and ions ($\chi_{e,i}$) are updated such that [37],

$$D^{\text{new}} = -\Gamma^{\text{SOLPS}}/\nabla_r n^{\text{EXP}}, \tag{2}$$

$$\chi_{e,i}^{\text{new}} = -\frac{q_{e,i}^{\text{SOLPS}} - \frac{5}{2}\Gamma T_{e,i}^{\text{SOLPS}}}{n^{\text{EXP}}\nabla_r T_{e,i}^{\text{EXP}}}, \tag{3}$$

where Γ^{SOLPS} is the radial particle flux at each grid cell from SOLPS, n^{EXP} is the experimental electron density, $q_{e,i}^{\text{SOLPS}}$ are the electron and ion radial heat fluxes from SOLPS, $T_{e,i}^{\text{SOLPS}}$ are the electron and ion temperatures from SOLPS, and $T_{e,i}^{\text{EXP}}$ are the electron and ion temperatures measured from the experiment. Experimentally measured gradients are taken to be purely in the radial direction, with upstream poloidal variation

assumed to be negligible by comparison along the Thomson scattering laser path. The goal of this iterative process is to match the profile gradient to the experimental measurement at each radial location of the SOLPS grid. Because this procedure relies on modifying diffusive transport coefficients alone, experimental profiles used as inputs must have a finite negative gradient throughout the profile. Transport coefficients for the private flux region (PFR) here are set to a constant value equal to the value of the first radial cell outside of the separatrix in the SOL. D and χ_i are set to be the same for all plasma species here.

If an existing set of transport coefficients are not available as a starting point, the standard procedure is to start with a reasonable estimate for radially constant diffusive transport coefficients (for example, $D \sim 0.05$ m^2 s^{-1} and $\chi_{\mathrm{e,i}} \sim 1$ for DIII-D). SOLPS is then run to convergence, and a new set of radially varying transport coefficients is generated according to equations (2) and (3). For each set of updated transport coefficients, SOLPS is run to convergence, at which point the SOLPS upstream plasma profiles are compared to the experimental measurements. If an improved match is desired, the radial transport coefficients are updated and SOLPS is run to convergence again. For the DIII-D cases presented here, a solution for the transport coefficients was determined to be converged if the updated coefficients closely matched the previous iteration, and T_e at the separatrix was within 1 eV of the experimental fit. This process generally converges SOLPS profiles to the upstream experimental conditions within experimental uncertainties in fewer than 10 iterations of updated transport coefficients when starting from a default input state. Fewer iterations are required when the initial transport coefficients are closer to the final solution. This process often requires manual intervention when, for example, the target density gets too low and the target electron temperature increases without bound. In such cases, choosing different initial conditions for the transport coefficients can be beneficial.

When particle flux boundary conditions are imposed at the core plasma boundary, iteratively solving equations (2) and (3) generally results in agreement between the profile gradients in SOLPS compared to the experimental profiles, but not necessarily agreement in the absolute values. This is a consequence of solving a 1D diffusion equation, where the gradient is the variable and a boundary condition is required to constrain the absolute values. In the case where experimental density and temperature profiles approach zero at the SOL grid boundary, this imposes an effective boundary condition at the SOL edge of the SOLPS profiles. For profiles with plasma grids that are somewhat radially truncated, as is the case here with tightly baffled divertor structures, the density and temperature at the grid boundary do not necessarily approach zero. Additional modifications can then be required to match the absolute values of each 1D plasma profile.

To address this offset, here we separately modify the transport coefficients of the final radial grid cell at the SOL boundary (the guard cell at the 'north' boundary) so that the transport off the plasma grid is either increased or decreased compared to the previous iteration in proportion to the mismatch between the boundary conditions, such that

$$D^{\mathrm{new}}|_{\mathrm{NB}} = D^{\mathrm{old}}|_{\mathrm{NB}} \frac{n_\mathrm{e}^{\mathrm{SOLPS}}|_{\mathrm{NB}}}{n_\mathrm{e}^{\mathrm{EXP}}|_{\mathrm{NB}}}, \tag{4}$$

$$\chi_{\mathrm{e,i}}^{\mathrm{new}}|_{\mathrm{NB}} = \chi_{\mathrm{e,i}}^{\mathrm{old}}|_{\mathrm{NB}} \frac{T_{\mathrm{e,i}}^{\mathrm{SOLPS}}|_{\mathrm{NB}}}{T_{\mathrm{e,i}}^{\mathrm{EXP}}|_{\mathrm{NB}}}, \tag{5}$$

where the NB subscript denotes that each quantity is evaluated at the north boundary and this transport coefficient is only being applied at that location, in the final radial grid cell in the SOL. Decay length boundary conditions were set to 3 cm for all quantities at the radial boundary of the 2D plasma grid, including all particle species as well as electron and ion thermal transport, but this iterative procedure converged to nearly identical plasma solutions when this length was changed to 1.5, 6 and 9 cm, where the only difference was a change in the transport coefficients in the final cell. This insensitivity of the boundary condition is a feature of using equations (4) and (5) with the iterative procedure, although as will be discussed later, the decay length should be set sufficiently high such that too much power is not lost off the grid in the early iterations. Because particles reaching the radial grid boundary remain in the simulation as neutrals, while energy is simply lost, equation (4) can be less effective at converging the simulation to the desired densities than equation (5) is at converging to the desired temperatures. Without these additional constraints, the profiles generally do not converge to the correct absolute values in cases like the ones presented here where temperature and density are not approaching zero at the radial edge of the grid.

In situations where a density shoulder is present in the far SOL [38], even an extended radial grid domain may be insufficient for the plasma density to reach a sufficiently low level at the radial grid boundary that the absolute density is easily matched without some enforcement. SOLPS has nonetheless been shown to reproduce critical features in such plasmas using a similar iterative transport matching procedure for particle flux [39]. There are also significant non-linearities in plasma parameters where the target is detached that can lead to challenges in converging transport coefficients using equations (2) and (3).

3.2. Particle flux scan

SOLPS simulations are presented in figure 2, varying the particle flux injected at the core boundary of the plasma domain. The calculated neutral beam fueling rate deposited in the core from the experiment was 7.14×10^{20} D atoms/s, so simulations were run with multiples of this quantity between 1 and 5 used as the deuterium particle flux injected at the core boundary. Because the measured pumped particle rate was approximately 3 times the neutral beam fueling rate, this equates to a range of 1/3 to 5/3 of the pumped particle flux. Transport coefficients were iteratively solved to match the experimental gradients in upstream profiles as a function of normalized poloidal magnetic flux ψ_N, based on the

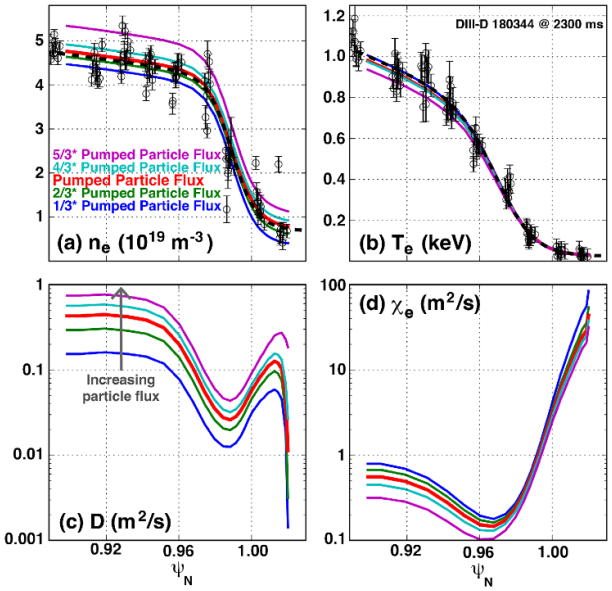

Figure 2. Upstream profiles of (*a*) electron density and (*b*) temperature, (*c*) particle diffusivity and (*d*) electron thermal diffusivity. Experimental measurements are presented as circles with errorbars in (*a*) and (*b*), and the experimental fits are plotted as black dashed lines. Colored lines denote SOLPS simulations, with particle flux injected at the core boundary varied from one to five times the experimentally injected values from NBI, where the experimentally measured pumped particle flux is 3 times the NBI particle source rate (baseline case in red).

experiment and setup introduced in section 2. Experimental measurements of n_e and T_e from Thomson scattering in the final 20% of ELM cycles are plotted as black circles with errorbars in figures 2(*a*) and (*b*), respectively, and fits to experimental data are shown with a black dashed line. These fits were used to iteratively modify transport coefficients in each case according to equations (2) and (3). Converged SOLPS simulations are then plotted as colored lines in each panel, including the corresponding diffusive particle and electron thermal energy transport coefficients in panels (*c*) and (*d*), respectively, that produced the simulated profiles.

As shown in figure 2(*a*), the resulting plasma density profiles were able to match the gradient of the experimental profile in all cases, but using core flux boundary conditions without an absolute density boundary condition results in most cases exhibiting a radially constant offset from the experimental profile. The measured particle removal rate in the experiment was approximately 3 times the experimental rate of particle injection by neutral beams (NBI), using calibrated measurements from a neutral pressure gauge [40]. This level of particle throughput (the experimental pumped flux) corresponds to the simulation profile that best matches the density profile with the decay length boundary conditions used here (red traces in figure 2). The simulation using the experimental particle removal rate as the particle throughput at the core boundary is therefore used as the baseline for other scans that will be presented later.

In every case, this iterative process of diffusive transport coefficient modification was able to match the experimental gradient well despite a factor of 5 difference in particle throughput. Again, this is a consequence of solving for the profile gradients in equations (2) and (3), and similar conclusions about this transport degeneracy with different particle fluxes have been reported in previous studies from JET [41]. The particle throughput has been shown in modeling to be critically important to the boundary plasma solution [42], suggesting that it may be preferable to impose a particle flux at the core boundary for the purposes of interpretive modeling of experimental discharges in cases with core fueling from neutral beams or pellets. Imposing a density at the core boundary results in the simulation injecting as many particles as necessary to match the density condition given the initially prescribed transport. When transport coefficients are iteratively solved to match experimental profiles, as they are here, these two free parameters (diffusivity and flux) result in a degenerate solution.

A major challenge with using core particle flux boundary conditions, however, is matching the separatrix density condition $n_{e,sep}$. As seen in figure 2(*a*), while the profile gradients are well-matched, $n_{e,sep}$ varies by nearly a factor of 2, which, in some combination with the change in particle throughput, has a substantial impact on downstream profiles, as will be shown in the next section.

SOLPS T_e profiles in figure 2(*b*) are well-matched with the experimental data in all cases. Ion temperatures were similarly well matched to fitted profiles of main ion charge exchange measurements of deuterium in each of these cases, an in-depth study of which is discussed later in section 5.2.

3.3. Downstream profile comparisons

Downstream plasma profiles measured by embedded Langmuir probes at the inner and outer divertor targets are compared against SOLPS solutions in figure 3 for the particle flux simulation scan with matched upstream profiles in figure 2. Ion particle flux profiles ('J_{sat}') are shown in panels (*a*) and (*b*), T_e profiles in (*c*) and (*d*), and poloidal heat flux profiles (q_{pol}) in (*e*) and (*f*). Colors correspond to the same simulations as figure 2, with the red case again representing core particle flux that approximately equals the measured particle exhaust rate (3 times the NBI particle injection rate). Voltage on the probes is swept such that T_e, n_e and ion saturation current (J_{sat}) measurements are available with a 1 kHz time resolution.

For the experimental data shown here, the marker represents the median data point in the time range of interest ($+/-$ 50 ms) while the errorbars denote one standard deviation in either direction, for both the measurement quantity and the probe location with respect to the reconstructed magnetic geometry ψ_N.

The wide variation in downstream plasma solutions in figure 3 highlights the importance of accurately reproducing $n_{e,sep}$ and properly modeling total particle throughput in boundary simulations. If core density boundary conditions are

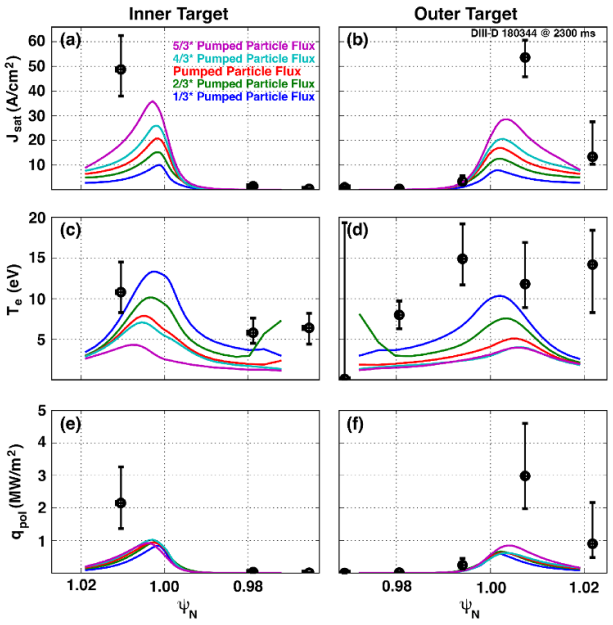

Figure 3. Profiles of $J_{\rm sat}$, $T_{\rm e}$ and $q_{\rm pol}$ at the inner and outer targets for the modeled core flux particle scan with matched upstream profiles (colored lines) compared with measurements from Langmuir probes (black circles with errorbars).

applied, it is critical to check that the final particle throughput through the core boundary is not deviating significantly from experimental expectations. If $n_{\rm e,sep}$ can be matched, particle flux boundary conditions may be preferable for neutral beam-heated plasmas to ensure physically relevant particle throughput and target plasma conditions.

Another conclusion that can be drawn from figure 3 is that across the entire range of particle fluxes that were modeled, the downstream ion flux, temperature and heat flux were all significantly lower than the measured quantities. The baseline case (where particle throughput matches the experimental pumped particle rate, plotted in red in figures 2 and 3) underestimates the ion flux to the target by more than a factor of 3 relative to the measurements from Langmuir probes. This is likely explained by a discrepancy in the modeling where insufficient power is being conducted to the target, which will be described in section 4.

Heat flux from Langmuir probe measurements is calculated assuming a sheath transmission coefficient $\gamma = 7$. The peak simulated heat flux is a fraction of that measured by Langmuir probes, which itself may not be the peak experimental value, since the spatial sampling here is coarse. Similarly, measurements from a toroidally-viewing infrared camera found the peak heat flux in the latter half of the ELM cycle to be approximately 2 MW m^{-2}, although the spatial resolution is poor compared to the simulations, and this is likely an underestimate of the true peak. At the same time, both the inner and outer heat flux profiles decay to less than 1/3 of their peak values at the SOL edge of the grid. This suggests that the radial heat flux profiles are not simply being widened to an extreme radial profile width that is truncated by the finite width of the grid. A similar conclusion can be drawn from other cases where a majority of heat flux is lost to the radial grid boundary, despite much wider radial grid domains [43].

4. Energy escaping radial grid domain

A challenge with the iterative transport coefficient matching process described in section 3 is that the transport resulting from fitting the experimental profiles often forces a significant fraction of the injected energy off of the plasma grid, in a way that conflicts with experimental observations and expectations. Energy exiting the grid on the 'north' boundary (at the radial edge of the SOL) in this way is simply lost in the simulation, assumed to be deposited on wall structures away from the divertor target within the plasma domain. This escape of energy off the simulation domain even occurs in cases when the grid extends many multiples of the heat flux width λ_q outside of the separatrix [20, 43]. This is not always a problem, as the profile matching has been found to be effective without disproportionate energy flux escaping the domain in many cases [37, 39, 44–47], but here we focus on a particularly challenging case that highlights the issue.

An example is presented in figure 4, which shows the poloidally-integrated radial particle flux in panel (*a*) and total plasma energy as a function of normalized poloidal flux $\psi_{\rm N}$ in panel (*b*). The subset of particle flux from D^+ ions is plotted in blue in panel (*a*), while the total electron flux is plotted in black (the difference is due to impurity carbon ion flux). In panel (*b*), the total energy flux is given in red, while the component resulting from convective flux is shown in magenta (equal to the sum of $2.5\Gamma_j T_j$ over all species *j*). Grid boundaries of the core and SOL are plotted as dashed black lines. The SOLPS simulation presented in figure 4 is the same as the baseline case plotted in red from figures 2 and 3, where the particle injection matched the measured pumping rate and upstream profiles matched most closely with the experiment.

As seen in figure 4(*a*), the D^+ ion flux that escapes the north boundary is 13.2% of the quantity of D^+ injected at the core boundary. This particle loss is an even smaller fraction when it is normalized by the ion flux through the separatrix (6.8%). The thermal flux in figure 4(*b*), on the other hand, can be seen to exhaust over 87% of the energy injected at the core boundary through the radial grid boundary at the SOL edge. The convective component is relatively small, accounting for less than 0.4% of the energy escaping the grid domain, so that the majority of energy is lost due to conduction. This level of radial energy flux leaving the simulation domain results in only a small fraction of the injected energy remaining to deposit on the target surfaces.

The experimentally reconstructed 2D radiated power profile measured by an array of bolometers [48] is plotted in figure 5. The location of the bolometer chords is shown in gray, and radiated power was averaged around 2300 +/− 20 ms, integrated through the ELMs. The radiated power profile calculated by the baseline SOLPS case (red traces from figures 2

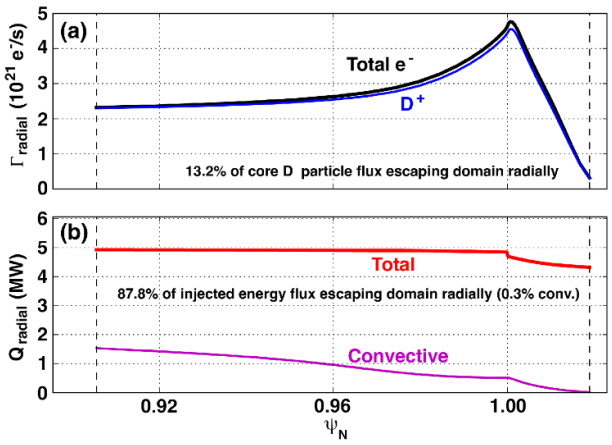

Figure 4. Poloidally-integrated radial flux of (*a*) D^+ particles and (*b*) energy, as a function of normalized flux on the SOLPS grid.

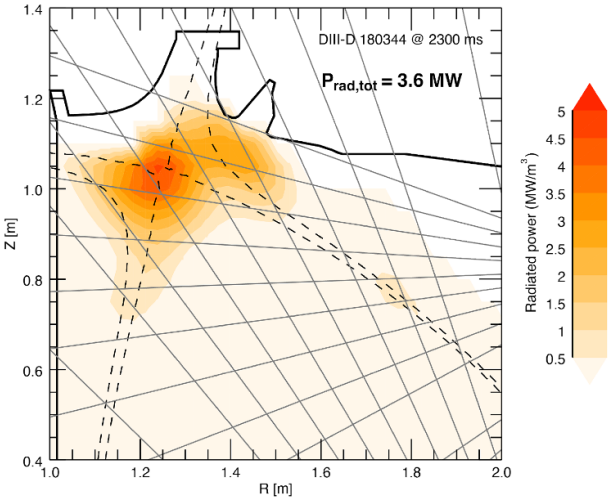

Figure 5. 2D reconstruction of radiated power in the upper DIII-D divertor from shot 180344 at 2300 ms. Bolometer chords are shown as gray lines.

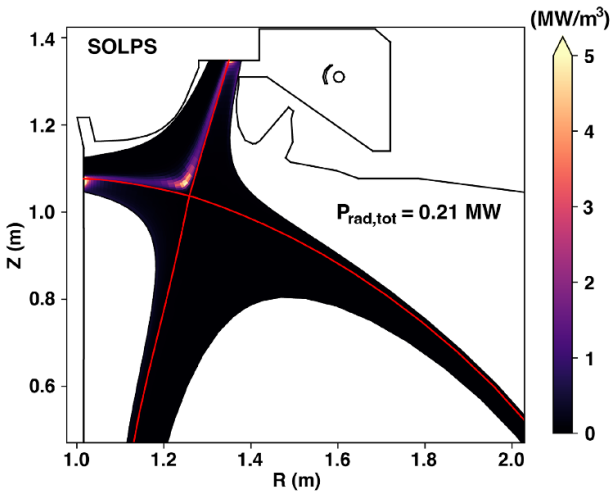

Figure 6. Radiated power profile calculated by SOLPS for the baseline case.

Table 1. Power sources and sinks in the plasma from the experiment and baseline SOLPS simulation. All power is in units of MW.

Source/Sink	Exp. (MW)	SOLPS
Injected power	6.15	4.92
ELMs	1.23	0
Radiated power	3.6	0.215
Inner target	∼0.5	0.12
Outer target	∼0.4	0.11
SOL bdy. (Upstream)	<∼0.4	4.185
SOL bdy. (Div.)	<0.4	0.12
PFR bdy	<0.4	0.0

and 3 is then shown in figure 6. The total radiated power estimated by the bolometer measurements was 3.6 MW, while the total integrated radiated power by SOLPS is only 0.21 MW. This is despite the fact that the majority of the experimentally reconstructed radiated power is located within the volume encompassed by the simulation domain, demonstrating that the simulation is missing the majority of this radiated power. While some of the experimentally measured radiated power likely came from emission during ELMs, the power from which is neglected in the SOLPS simulations, the total power ejected by ELMs was only ∼1/3 of the radiated power measured in the experiment here, so ELMs are not the dominant source of disagreement between the simulation and experiment. About 80% of the radiated power in the simulations comes from carbon species, which is roughly consistent with previous experimental studies using calibrated reconstructions of the 2D emissivity in the lower divertor of DIII-D [49, 50].

Finally, table 1 provides the power balance analysis for the plasma from both the experimental observations and the baseline SOLPS simulation. Power lost to the simulation radial grid boundary, denoted 'SOL bdy' in the table, is broken up into the component lost 'Upstream' (in the main chamber) and that lost in the divertor region of the SOLPS grid ('Div.'). Because there is no experimental measurement of these quantities, it is simply noted that the power leaving these regions in the experiment must be less than the remainder of the other terms in the power balance. The radiated power measurement is integrated through the ELM cycles, so there may be some double counting of experimental power that is radiated and what is estimated to be lost to ELMs. The experimental estimate of heat flux to the targets is a very rough estimate based on scaling up the SOLPS target fluxes from figure 3 to match the relatively sparse data from Langmuir probes.

The poloidal dependence of heat flux density escaping the simulation domain in the SOL is plotted in black in figure 7, using the left figure axis. The poloidal distance along the radial grid boundary is measured starting from the outer divertor target, passing through the SOL and ending at the inner divertor target. The location of the outboard midplane is labeled 'OMP', and poloidal index of the X-point is identified at the entrance of each divertor. The inverse of the outer-most radial cell width is then over-plotted in blue using the right axis. The heat flux density is largest near the OMP, with

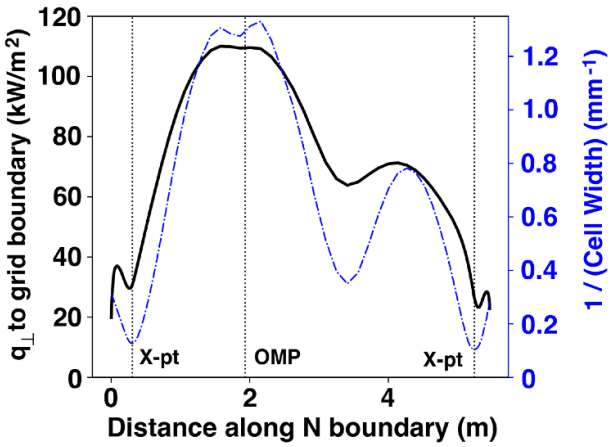

Figure 7. Power escaping the simulation domain in the radial direction as a function of the poloidal location along the SOL radial boundary (in black, left axis), along with the inverse of the outer-most radial cell width (in blue, right axis).

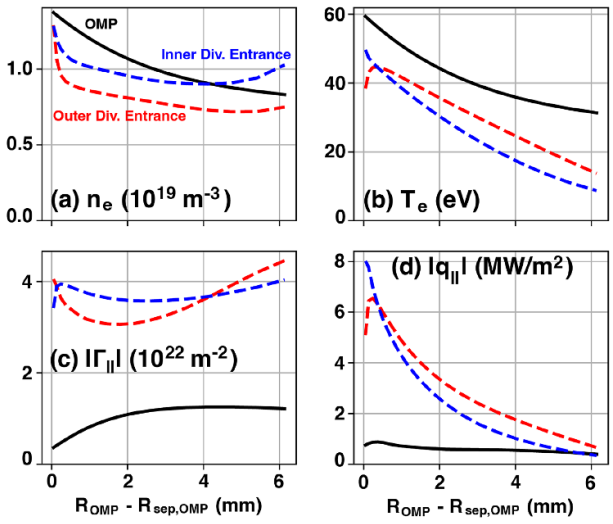

Figure 8. Simulated radial profiles in the SOL of (*a*) n_e, (*b*) T_e, (*c*) $|\Gamma_{||}|$, and (*d*) $|q_{||}|$ for poloidal positions at the outboard midplane (OMP, solid black) and inner and outer divertor entrances (dashed blue and red, respectively) in the baseline case. Radial positions and cell areas are mapped to the outboard midplane.

a secondary peak near the inboard midplane. This correlates strongly with the inverse of the radial cell width, which might be expected for poloidally similar temperatures, where the diffusive thermal flux is proportional to the local radial temperature gradient. The thermal transport is driven more strongly in regions of strong flux compression due to the increase in temperature gradients when the radial cell-to-cell distance is reduced, even using poloidally symmetric transport coefficients.

The resulting simulated SOL radial profiles for n_e and T_e are plotted in figures 8(*a*) and (*b*) for three poloidal locations with the baseline case of the particle flux scan: the 'OMP' (plotted in black) and the inner and outer divertor entrances (dashed blue and red, respectively). For all poloidal locations, the radial coordinate is mapped to the radial distance from the separatrix at the OMP. The absolute value of the parallel flux densities of particles ($\Gamma_{||}$) and energy ($q_{||}$) are then plotted in panels (*c*) and (*d*), respectively, for the same poloidal locations. The perpendicular cell areas that are used to calculate these parallel flux densities are again mapped to the OMP to normalize for flux expansion.

The poloidal variation of n_e and T_e profiles in the SOL in figure 8 is indicative of large radial transport with the significant poloidal variation shown in figure 7. Longer decay lengths for T_e and $q_{||}$ on the outboard side compared to the inboard side in figure 8 is also consistent with the poloidal variation seen in figure 7. It is important to note that the standard understanding of a single scaler quantity λ_q that describes the energy decay in the SOL is dependent on relatively constant values of both D and χ, as well as a small fraction of power escaping the domain, neither of which elements are present here.

The implication of the simulation data presented in this section so far is that, while the particle diffusivity D derived using the iterative process to match upstream plasma profiles in section 3 seems reasonable (because relatively few plasma particles escape the simulation domain radially, and convective energy flux is not dominant), the thermal diffusivity χ appears to be too large. Approximately half of the 'missing' radiated power might be a result of the 'radiation shortfall' that is often attributed to the effect of molecules that are improperly modeled in a carbon-walled device [44], but the radiation here is too low by much more than a factor of two. Furthermore, both the radiation and parallel conduction terms are underestimated by the simulation, as a majority of the power is conducted radially to the SOL edge in the main chamber before it can reach the divertor. However, according to the iterative procedure, this was the value of χ_e that was required to match the electron temperatures that were measured upstream.

Several approaches have been taken to attempt to address this apparent excess in radial thermal transport, which will be discussed in the next subsections.

4.1. Setting a max value for χ

Given the extreme values of χ in the far-SOL, one potential solution to minimize the energy escaping the grid is simply to set a maximum value for χ_e and χ_i as transport coefficients are iterated. Figure 9 shows profiles of (*a*) n_e, (*b*) T_e, (*c*) particle diffusivity D and (*d*) χ_e, starting with the baseline case in red, then doing a single simulation where only the values of χ greater than 10 m^2 s^{-1} are reduced to 10 m^2 s^{-1} everywhere except the boundary where equation (5) was applied (shown in green), another single simulation where $\chi \leq 10$ m^2 s^{-1} everywhere, including the boundary (shown with a dashed brown line), and a final case where the iterative profile fitting process was run to completion, maintaining $\chi \leq 10$ m^2 s^{-1} everywhere throughout the process (shown in solid purple). Experimental Thomson scattering data is plotted with errorbars in panels (*a*) and (*b*), and the profile fits are plotted as dashed black lines. The radial coordinates in figure 9 are focused on the region near the separatrix and in the SOL, since this is where the transport changes are made. The value for χ_i was also limited

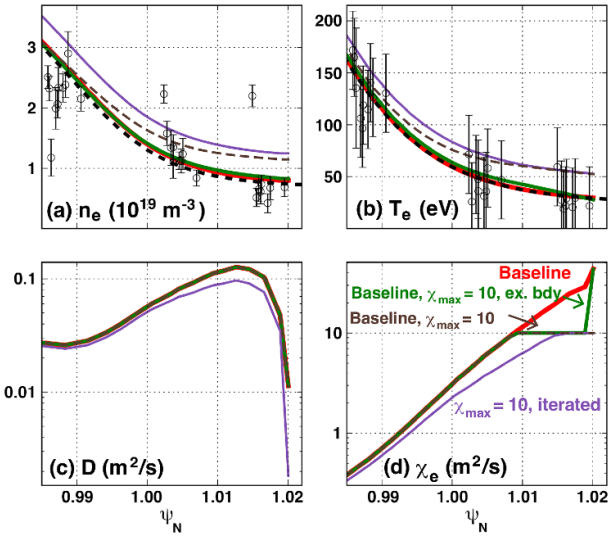

Figure 9. Edge profiles of (*a*) n_e, (*b*) T_e, (*c*) D and (*d*) χ_e, for the baseline case (solid red), the same case with $\chi_{max} = 10$ m^2 s^{-1} (dashed brown), the same case again with $\chi_{max} = 10$ m^2 s^{-1} everywhere except the north boundary (green), and a case where the iterative process was run to completion for the whole profile, maintaining $\chi \leq 10$ m^2 s^{-1} (solid purple).

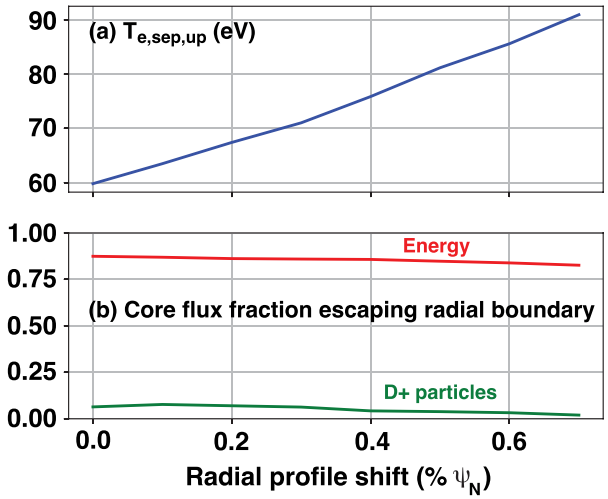

Figure 10. (*a*) Upstream separatrix electron temperature and (*b*) the fraction of energy (red) and D+ particles (green) injected at the core that escape the radial grid boundary with varying radial separatrix shifts to the fitted experimental profiles.

to 10 m^2 s^{-1} for the same cases as χ_e, but this only impacted the final cell at the north boundary (set by equation (3)).

Setting this maximum value for χ succeeds in retaining more of the power in the simulation domain, but most is still lost. While ∼87% of the power escapes the radial grid boundary in the baseline case, ∼80% escapes for the same simulation with $\chi_{max} = 10$ m^2 s^{-1}, and ∼75% escapes following several further iterations of transport coefficients to match the profile gradients throughout the domain. As seen in figure 9, however, these modifications also lead to a mismatch between the simulations and the measurements in the SOL. In particular, both n_e and T_e deviate significantly from the target values at the separatrix. Removing the constraint and then iterating starting from these simulations with more of the energy remaining in the simulation domain results in energy being again transported off the grid, converging back to a similar solution as the baseline case. When the max χ constraint is applied everywhere except at the north boundary (green lines in figure 9), the profiles match relatively well with only a slight increase in temperature and density across the SOL, and the power escaping the domain is slightly reduced to 84%. This shows the importance of the boundary conditions defined by equations (4) and (5), although it may be beneficial to avoid updating the boundary condition for χ in early iterations of the procedure so that excess power off the grid is not baked in to future iterations.

4.2. Radial shift of experimental separatrix location

One of the most significant factors in determining power conducted to the target in the parallel direction is the separatrix electron temperature, $T_{e,sep}$ [51]. For the particle flux scans shown in section 3, $T_{e,sep}$ was approximately 60 eV (as seen in figure 2(*b*)), while power balance analysis of this discharge [52] suggests that $T_{e,sep}$ should be in the 80–95 eV range.

To explore the impact that $T_{e,sep}$ has on the energy escaping the simulation domain through the radial grid boundary, a scan was performed to radially shift the experimental profiles and iteratively solve the transport coefficients for each new set of fitted profiles, as outlined in section 3. The results of this scan are presented in figure 10, where the upstream electron temperature at the OMP separatrix is plotted in panel (*a*) and the energy and main ions that escape the simulation domain in the radial direction are plotted in panel (*b*), as a fraction of each quantity that is injected at the core boundary.

As shown in figure 10, shifting the separatrix outward provides only a moderate reduction in the energy escaping the radial grid boundary, despite a much larger $T_{e,sep}$.

4.3. Ballooning transport

Another possible explanation for the excess energy escaping the grid radially is that the experimental profiles being matched are poloidally located on the outboard side of the tokamak. If transport in the experimental SOL was sufficiently poloidally asymmetric, these measurements would not be representative of the full poloidal average and therefore would not be captured by the one-dimensional assumptions of the poloidally symmetric transport coefficients and iterative scheme presented in section 3.

SOLPS-ITER has the built-in functionality to modify transport coefficients poloidally depending on the local magnetic field at each cell, in an attempt to reproduce ballooning-like transport that is larger on the low-field side of the device. With

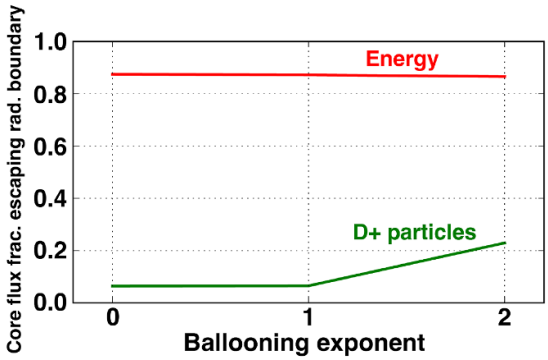

Figure 11. The fraction of energy (red) and D+ particles (green) that escape the radial grid boundary with varying ballooning factors applied to transport coefficients.

this option enabled, the diffusive transport coefficient at each cell poloidally D_{local} is modified by

$$D_{\text{local}} = \left(\frac{\langle|B|\rangle}{|B|}\right)^{n} D_{\text{rad}}, \tag{6}$$

where $|B|$ is the local magnetic field strength in the center of each cell, $\langle|B|\rangle$ is the average of this value over all of the cells in the 2D plasma domain, n is the exponent assigned by the user for the ballooning term, and D_{rad} is the transport coefficient for the radial index as calculated here by equations (2) and 3. A similar modification is made to thermal transport coefficients χ_{e} and χ_{i}.

To examine the influence of poloidally asymmetric diffusive transport on the energy escaping the grid in these simulations, ballooning transport coefficients were used for the baseline case here. Transport was iteratively modified to match upstream profiles according to the procedure in section 3 with the ballooning exponent n in equation (6) set to 1 and 2, which can then be compared to the baseline case where it was zero. Following the iterative procedure, upstream electron density and temperature profiles for each of the three cases match well with the fitted measurement profiles at the poloidal position of the Thomson scattering laser path ($T_{\text{e,sep}}$ is within 2 eV, and density profiles have a maximum offset between the three cases of 0.05×10^{19} m^{-3}). The resulting energy and particle flux escaping the grid across this scan is presented in figure 11. This scan shows that there is only a $\sim$1% reduction in the energy flux escaping the radial grid for the values of ballooning transport explored here. Attempts at converging cases with larger ballooning exponents were unsuccessful.

4.4. Potential solutions to be explored

Several other potential solutions to the problem of too much energy escaping the grid in the radial direction were considered as part of this work, but have not yet been fully explored. One modification would be to add the effects of cross-field drifts, which changes the radial transport and may impact the fluxes that escape the domain. A few simple, low-effort improvements would be to only update the particle diffusion coefficients during the first few iterations of the procedure until the density profile is at least somewhat converged before modifying thermal transport, or to keep χ at the north boundary below some prescribed level for the early iterations. The hope in both cases would be to prevent excess power from being transported radially in early iterations of the procedure when the upstream profiles differ significantly from the experimental fits.

Another observation is that there is a path dependency to keep thermal flux from leaving grid, such that once there is a given amount of thermal energy flux being transported radially, this can to some extent be 'baked in' to the iterative procedure through the term $q_{\text{e,i}}^{\text{SOLPS}}$ in equation (3). Therefore, starting with lower values of χ in the initial simulation with constant transport coefficients might theoretically minimize the thermal flux escaping the grid in the first iteration by increasing the temperatures and driving more thermal flux to the divertor targets. In the case presented here, this was attempted, but was not successful at reducing the energy leaving the grid domain in the final converged state. It is likely a necessary but not sufficient piece of the solution. Manually reducing χ in the far SOL between iterations was also unsuccessful at resetting the evolution of the transport coefficients, although the details of these changes are likely important, such that further attempts might achieve different results.

A case with the same inputs but using constant values of $D = 0.3$ and $\chi = 1.0$, modeled after predictive simulations from ITER [53], resulted in 39% of the power escaping the grid, while the n_{e} and T_{e} profiles were significantly mismatched, with $n_{\text{e,sep}}$ more than twice the targeted experimental value. Manually modifying the constant transport coefficients to find a better match with experimental profiles before beginning the iterative procedure may produce an improved match in the end.

The boundary conditions at the north boundary could be changed from decay length to some other function, although leakage boundary conditions are effectively the same for given plasma background, so we would not expect this to change the fundamental challenge. This was not attempted here, but it could be a factor in sending the iterative procedure on the wrong path if this boundary condition pulls more heat flux toward the radial grid boundary.

A more physics-based solution to this transport problem could be to assume that transport is convective rather than diffusive, particularly in the far SOL, and solve for the convective particle velocities rather than diffusion coefficients that were used in equations (2) and (3), while maintaining some finite diffusivity for numerical stability. Since transport in the far-SOL is likely dominated by convective blobs rather than diffusion [38, 54, 55], this may enable an improved match to experimental profiles without forcing so much energy off the grid. Further inclusion of more physics-based transport models could be effective [28], but this likely requires more development than the other short-term solutions suggested in this section. An even shorter-term change would be to add a

finite outward convection term in the SOL so that the thermal diffusivity might not need to reach such extreme values in the far-SOL.

Alternatively, it may help to try to use different fitting parameters than the tanh functions that are usually used for DIII-D pedestal and edge profile fits [56], which are used to approximate a smooth fit to the experimental data before applying it to the fitting procedures in equations (2) and 3. A more brute force tactic could be to concede that the conditions in the far SOL are not properly described by either a simple Maxwellian distribution function in each cell or by a diffusive model, such as if they are 'blob-y'. One could then modify the experimental electron temperature profiles in the far SOL, for example, by applying an additional exponential decay beyond a few heat flux widths outside the separatrix. Modeling efforts could then be focused on accurately describing the system near the separatrix.

The problem of matching experimental plasma profiles with fluid boundary plasma modeling without forcing excessive energy radially off the grid is a challenge [20, 43], and there are likely other potential solutions not discussed here.

5. Additional considerations for realistic neutral physics

Several other considerations that are frequently neglected in boundary modeling will now be addressed, to demonstrate their importance to more accurately reproduce the physical system. The physics of pumping plenum geometry and ion temperature each impact the modeled neutral physics and therefore recycling and ionization profiles, which will be explored here. The influence of other less-commonly modified model inputs, such as the core rotation boundary condition, have been shown elsewhere to influence the plasma solutions from SOLPS [57].

5.1. Inclusion of a thermalizing plenum volume

A common simplification used in interpretive boundary modeling simulations is to approximate pumping at a surface near the opening of the pump plenum, [22, 41] thus avoiding the complexity of adding more neutral volume to the simulation, which can increase computational time and potentially complicate convergence. In regions where the neutral population is sufficiently thermalized so that the majority of particles being removed from the simulation are equilibrated to the temperature of the wall, equation (1) would be sufficient to calculate the pumped particle fraction that reproduces the volumetric pumping rate. For cases where the neutral velocity $\bar{v}$ incident on the absorbing surface changes because the neutral energy spectrum changes, however, this assumption breaks down, and a more complete representation of the pumping geometry may be required to capture the physics of thermalization and molecule formation that takes place in the pump duct and plenum volumes [58–60]. This is often the situation when there is a clear line of sight and relatively large solid angle between the divertor target where neutral particles are born and the pumping surface in the EIRENE grid.

In order to test the necessity of including a plenum geometry in the cases presented here, transparent surfaces were added to the EIRENE grid to quantify the effective pumping rate at two locations in the simulation grid that might have been used in lieu of the full plenum volume: one at the back of the pump duct, and one at the front, closest to the plasma. Pumping on the plasma end of the pump duct would be similar to applying particle removal on the edge of the plasma grid itself, for example what is used to remove fluid neutrals in UEDGE [4, 19]. The plenum geometry is shown in figure 12, along with the transparent surfaces denoted by a red line at the back of the pump duct and a green line at the front of the duct near the edge of the plasma grid. The cryopump ring is shown in blue, which are the only surfaces where particles are removed from the simulation. All D particles are injected into the simulation at the core plasma boundary, and they are all removed by the cryo pump ring, with 100% particle recycling on all other surfaces, so that all net flow of particles passes through both the red and green surfaces.

The effective pumping rate at each transparent surface is then plotted as a function of the total atomic D particle throughput of the system in figure 13. These calculations are based on the particle flux scan simulations from section 3.2, where the core particle flux and transport coefficients are modified for each level of particle throughput, while other model inputs are kept constant. The pumping rate of the surfaces of the cryopump is set to 0.168, as calculated by equation (7) using the experimentally calibrated volumetric pumping rate and the total surface area of these segments. The effective pumping rate $f_{\text{pumped,eff}}$ plotted as solid lines in figure 13 is calculated as

$$f_{\text{pumped,eff}} = \frac{N_{\text{D,in}} - N_{\text{D,out}}}{N_{\text{D,in}}}, \tag{7}$$

where $N_{\text{D,in}}$ and $N_{\text{D,out}}$ are the total number of deuterium atoms passing into and out of the pumping volume, respectively. This includes the contribution of two D atoms from each D_2 molecule. This number represents the pumping rate that should be applied to a surface at each position to replicate the volumetric pumping rate of the more-realistic pump with a thermalizing plenum volume. The effective pumping fraction is lower for the surface on the plasma side of the duct because of particles that enter the pump duct and then return to the main chamber following some collision rather than entering the plenum volume. Errorbars in figure 13 indicate the standard deviation of the calculated pumping rate from 50 time steps in this converged simulation, to give a sense of the statistical noise of the system including Monte Carlo neutrals. Figure 13 also includes dashed lines denoting the pumping rate that would have been applied at each position if equation (1) was applied assuming that all particles are D_2 molecules thermalized to the wall temperature (300 K here).

When a thermalizing plenum volume is included in the simulation, including a plate to prevent direct pumping of incoming energetic atomic particle flux on the cryo ring, nearly all particles are thermalized to the wall temperature (300 K here)

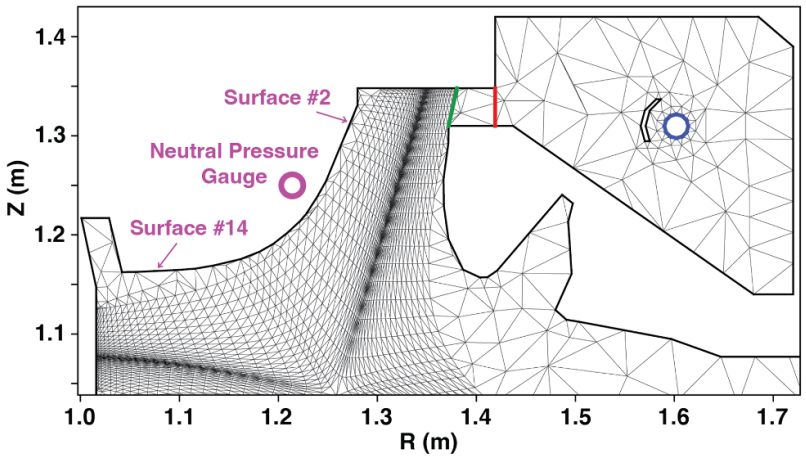

Figure 12. Modeled plenum geometry using an approximation of the pumping plenum and cryo pump (shown in blue), with green and red lines denoting transparent surfaces used for diagnosing the impact of different pumping models. Surface numbers and location of the pressure gauge in the PFR are labeled in magenta for reference for figure 15.

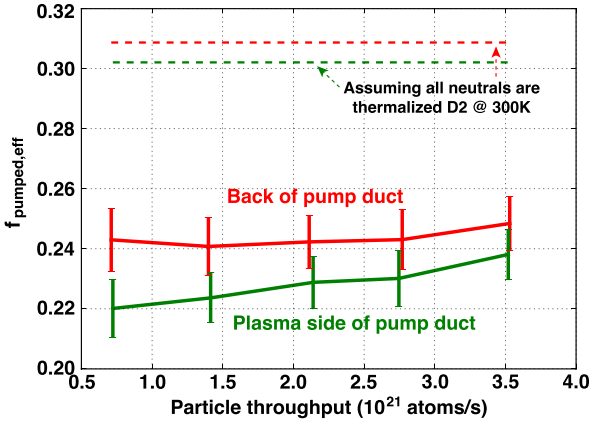

Figure 13. Effective pumping rate for the transparent surfaces labeled in figure 12 that would be required to match the desired volumetric pumping rate at each position in the absence of a thermalizing plenum volume. Solid lines are based on the simulated particle fluxes in and out of the plenum, while dashed lines denote the value calculated assuming all particles are thermalized molecular deuterium.

by the time they contact the pumping surface and are removed from the system. This physics replicates that of the real pump plenum and the pumping rate can be calibrated to the measured volumetric pumping rate according to equation (1) (where $S_{\mathrm{pump}} = 40\ \mathrm{m}^3\ \mathrm{s}^{-1}$ here). Without this volume, some estimate must be made about the average neutral particle velocity incident on the pumping surface. Because this is not known *a priori* before the simulation, the necessary pumping rate that should be applied to the surface (i.e. $f_{\mathrm{pumped,eff}}$) changes depending on the plasma and neutral population near the pumping surface.

As shown in figure 13, using equation (1) assuming a thermalized molecular deuterium particle flux, if the plenum volume were not included in this simulation and particle removal were instead applied at these proxy pumping surfaces, the particle removal rate might have been overestimated by roughly 1/3. Moreover, the 'true' particle reflection coefficient that should be set at each surface can change with plasma conditions, such that no single value would be valid across a wide range of conditions, although a suitable value may be sufficient for a given scan.

When these same simulations were run using a pumping surface at the back of the pump duct (the location of the red line in figure 12) with an absorption fraction calculated assuming an average energy distribution of D_2 at 300 K, following the iteration procedure to match upstream profiles, the target ion flux was reduced by about 15% relative to the case with the plenum volume included. This further demonstrates the sensitivity of the simulated pumping geometry when the target is positioned near the pumping surface(s), especially when there is line-of-sight with an attached target. It also highlights the role of kinetic neutral physics in the simulation.

5.2. *Treatment of ion temperature*

In the absence of reliable ion temperature measurements or understanding of the differential thermal transport between electrons and ions, a common simplification in interpretive boundary modeling is to assume that either $T_{\mathrm{i}} = T_{\mathrm{e}}$ or that $\chi_{\mathrm{i}} = \chi_{\mathrm{e}}$ [43, 45, 47, 61, 62]. In many cases this assumption may be invalid near or outside of the separatrix, however, where T_{i} has been measured to be two or more times the electron temperature in multiple devices [63, 64]. Here we investigate the implications of various assumptions of ion temperature on the simulated plasma and neutral system.

Impurity ion temperature measurements from fully stripped carbon C^{6+} are regularly available in DIII-D using CER [65]. More recently, main ion CER measurements have become available to directly measure the temperature of deuterium ions [64, 66]. In the core of the plasma, the impurity and main ion temperature measurements tend to be coupled so that $T_{\mathrm{D}} \approx T_{\mathrm{C6+}}$, while at the edge, they become decoupled due to differential transport and ionization profiles, as well as measurement idiosyncrasies related to the large trapped orbit widths

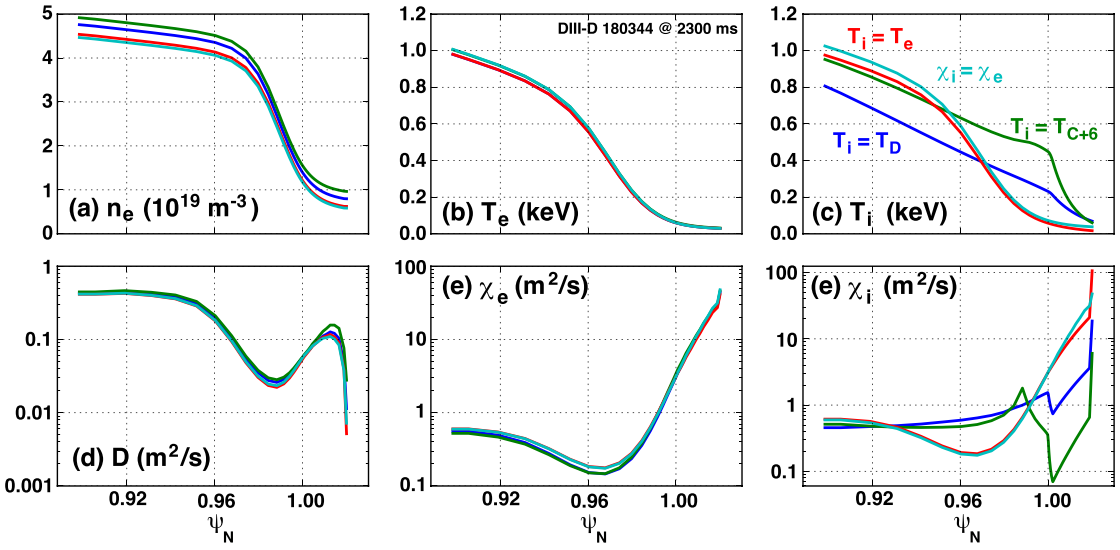

Figure 14. Modeled upstream profiles of (*a*) n_e, (*b*) T_e and (*c*) T_i and associated diffusive transport coefficients (*d*) *D*, (*e*) χ_e and (*f*) χ_i following transport coefficient fitting for various assumptions of ion thermal transport, labeled in panel (*c*).

of impurity carbon ions. Although the quantitative contribution from each of these two effects (real differences in T_i and measurement challenges with T_{C6+}) remains uncertain, the T_D measurements are more reliable in the edge when they are available.

In SOLPS, all ion species are represented with the same temperature T_i, although the thermal transport coefficient χ_i can be set differently for each charge state of each species. Here we assume that χ_i is the same for all ion species, which is necessary for a unique solution to equation (3) without additional information relating their relative values.

Figure 14 shows the simulated plasma (*a*) electron density, (*b*) electron temperature and (*c*) ion temperature upstream profiles for four cases: one where χ_i was modified so that T_i matched T_D from main ion CER measurements (this is the reference case from section 3, plotted in blue), one where χ_i was modified to attempt to match T_i with T_{C6+} from impurity CER (plotted in green), one where the transport was iterated assuming $T_i = T_e$, and a final case where χ_i was simply matched to the derived value of χ_e on every iteration. Resulting transport coefficients are then given in panels (*d*) for particle diffusion *D*, (*e*) for χ_e and (*f*) for χ_i. In the two cases that attempted to fit ion temperature profiles, a decay length of 0.015 in ψ_N space was imposed on the measured profiles outside of the separatrix, since ion temperature measurements are less reliable in the SOL.

As shown in figure 14, the assumption that $T_i = T_e$ was similar but not identical to the case where χ_i was set to equal χ_e. The case where T_i was matched to the T_D measurement approximates the measurement reasonably well near the separatrix: measured deuterium temperature at the separatrix $T_{D,sep}$ is approximately 250 eV, while SOLPS finds $T_{i,sep}$ to be 232 eV. Modifying transport coefficients to match upstream ion temperature profiles using T_i from impurity CER measurements, on the other hand, does not converge well, but the closest match is presented in figure 14. This simulation resulted in $T_{i,sep} = 449$ eV, where the measurement indicated that $T_{C6+,sep} \approx 600$ eV. This discrepancy (and the more general difficulty in achieving convergence to the experimental profiles) is likely because the electrons and ions are relatively collisional in the edge plasma where temperatures are lower, so iteratively modifying the diffusive transport coefficients alone to decouple T_e and T_i is a challenge.

The energy escaping the computational domain in the radial direction changed as the treatment of ion thermal transport was modified. While 87% of the power escaped the grid in the baseline case where T_i was matched with T_D, 78% was lost when χ_i was reduced to match T_i more closely with T_{C6+}. For the cases where the ion thermal transport was matched with electron temperature profiles, $T_i = T_e$ and $\chi_i = \chi_e$, 94% of the injected power was transported off the radial grid boundary. Higher ion temperature at the separatrix therefore corresponds to less power escaping the domain.

One of the most significant changes resulting from these modifications to the ion thermal transport was to the neutral particle population. The modeled neutral pressure incident on wall surfaces in the PFR is plotted in figure 15, along with the value measured by ASDEX-style neutral pressure gauges [40, 67] in the approximate sampling region.

The surface numbers on the *x*-axis denote surface segments of the 'dome' structure in the PFR on the SOLPS grid, ranging from 2 nearest the outer target to 14 nearest the inner target, as labeled in magenta in figure 12. Gray bands represent the maximum and minimum measurements from 2200 to 2400 ms. This variation represents the ELM cycles in this H-mode discharge, where the neutral pressure peaks shortly after an ELM and reaches a minimum just before the next ELM deposits more neutral particles in the divertor.

The primary result highlighted in figure 15 is simply that the ion thermal transport, which is often assumed to be identical to electron thermal transport, can have a significant impact on the downstream neutral solution and therefore the

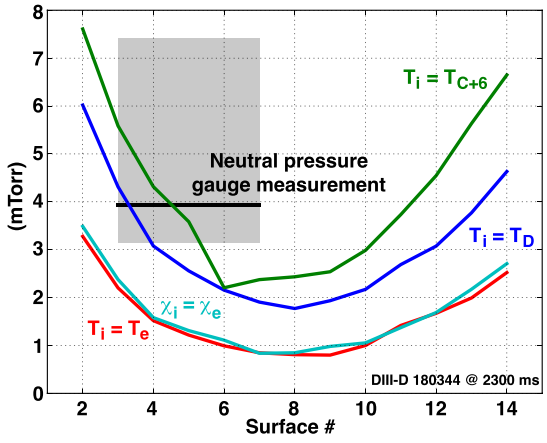

Figure 15. Modeled neutral pressure along wall surfaces in the private flux region (labeled in figure 12) for various assumptions of ion thermal transport, along with the corresponding measurement from a neutral pressure gauge positioned behind these tiles.

downstream ionization and plasma profiles when it is matched more closely with experimental measurements. Higher ion temperature upstream results in higher neutral velocities following charge exchange or fast reflection events, which can then penetrate more deeply into the plasma before being ionized. This suggests that the predictive capabilities of these simulations would benefit from an increase in focus on ion thermal transport, separate from and in addition to electrons, which we know from experiments are very different.

6. Discussion and future directions

The degeneracy of solutions to the transport equations and iterative solving procedure presented in section 3 suggests that the core particle injection rate should be constrained in simulations, while matching the separatrix density to experimental values as closely as possible. For similar reasons of reproducing particle balance, the particle removal rate of simulated wall elements should be represented as accurately as possible, including any absorption or outgasing effects, informed by calibrated experimental measurements of particle balance and volumetric pumping rates. The results of the plenum volume study show that, when a divertor target is positioned near a pump duct, including some thermalizing neutral volume in the simulation is necessary to approximate the desired volumetric pumping rate. Without this, the pumping rate on a surface cannot be known without forward knowledge of the average velocity of the incoming neutral particles, according to equation (1). A plenum volume of the size and detailed complexity included in the simulations here is likely unnecessary, however, as long as the effective neutral conductance between the incoming neutral flux and the pumping surface(s) is dominated by the volumes included in the simulated neutral domain.

Wide grids incorporated into SOLPS-ITER will enable modeling of the far-SOL and plasma interactions with the main chamber wall [24], which would improve both the physics and computational fidelity of the simulations. However, without a realistic model of plasma transport in this newly included far-SOL region, the model will continue to fail to reproduce physical processes in the near-SOL. Even very wide grids relative to the heat and particle flux widths have been shown to exhibit the problem of heat flux escaping the grid radially when transport coefficients are iterated with the method used here [43], suggesting that transport throughout the SOL needs to be resolved so that the energy decays in the near-SOL. This other example was able to match experimental target profiles much more closely than what was achieved here in section 3, though, which may indicate that the simulation in that case with a density shoulder and most power escaping by convection was missing some dissipated or deposited power somewhere. In addition to some of the simpler ideas discussed in section 4.4, another potential solution to this problem that has been developed recently is to use a model of electrostatic turbulence to approximate diffusive transport coefficients at all locations in the 2D SOLPS grid [28]. This particular method captures both ballooning characteristics and $E \times B$ suppression. It also has the advantage of being easily incorporated into the existing SOLPS-ITER framework. However, by assuming that this one transport mechanism is dominant, asserting that it is purely diffusive in nature, and attempting to calculate the radial electric field self-consistently without additional kinetic plasma effects, even this much-improved model is likely to be incomplete.

Recent experimental and modeling progress provides hope for a tractable path forward for approximating the blob-y transport in the far-SOL using fluid codes such as SOLPS-ITER. Measurements in TCV have correlated an increase in the density in the far-SOL with the neutral particle density [68]. This is consistent with recent full-f gyrokinetic modeling that finds that including the effects of neutral particles flattens the saturated density profile in the far SOL [69]. It remains to be seen whether this advanced understanding can be reformulated into simplified equations that can be expressed with sufficient accuracy in a fluid code such as SOLPS-ITER so that it can sufficiently approximate experimental observations. In the meantime, diffusive boundary plasma modeling may provide its most useful insights when focused on resolving the physics in the near-SOL region.

7. Summary and conclusions

Simulations have been presented using the SOLPS-ITER code to analyze experimental plasma and neutral conditions from a DIII-D experiment in a relatively closed, pumped divertor configuration. By iteratively modifying diffusive radial transport coefficients, simulations are shown to match experimental upstream electron temperature and density profiles over a range of values of core particle flux. Downstream, these different particle fluxes result in significant changes to the plasma flux at the divertor target. This highlights the importance of accurately reproducing the experimental particle throughput

in simulations, even if upstream conditions are otherwise matched.

When transport coefficients were iteratively solved to match measured upstream profiles, a majority of the plasma energy was shown to escape the radial simulation domain. This simulation result is in contrast to radiated power measurements and embedded Langmuir probes from the experiment, and despite the simulation grid encompassing ∼2–3 heat flux widths, using both the modeled width and the experimental profiles at the target to assess these scales. Shifting the separatrix location of the fitted experimental profiles to better match the expected value of T_e at the separatrix based on power balance assumptions did not significantly reduce the power escaping the grid, nor did the inclusion of ballooning transport coefficients. This conflict is partially attributed to the radial flux being somewhat 'locked in' during the iterative process, but manual modification of the thermal transport coefficients was unsuccessful at keeping more of the energy in the simulation domain, potentially suggesting more fundamental disagreements with the diffusive transport model being used to fit to the experimental data, particularly in the far SOL.

With the divertor target placed near the pump duct, a thermalizing plenum volume is shown to more robustly simulate the particle removal rate than a simple pumping surface placed near the pump with a fixed particle reflection coefficient. Without the thermalizing volume, the fractional particle absorption on the pumping surface that would replicate the experimental volumetric pumping rate is unknown *a priori*. Different assumptions of the ion thermal transport is also shown to modify the downstream neutral particle population, highlighting the importance of accurately representing this quantity in the simulations independent of the electron thermal transport.

These findings provide some avenues to improve boundary simulation capabilities, while informing best practices for using these computational tools most effectively as they presently exist.

Acknowledgments

The authors would like to thank Ivan Paradela Pérez for development and support of the Quixote software package for analyzing the output of SOLPS simulations, as well as Peter Stangeby and Filippo Scotti for fruitful discussions during the drafting of the manuscript, and finally the late Jon Watkins for his development and support of the DIII-D embedded Langmuir probes for many years preceding this work.

This material is based upon work supported by the U.S. Department of Energy, Office of Science, Office of Fusion Energy Sciences, using the DIII-D National Fusion Facility, a DOE Office of Science user facility, under Awards DE-AC05-00OR22725, DE-AC02-09CH11466, DE-AC52-07NA27344 and DE-FC02-04ER54698.

ORCID iDs

R.S. Wilcox 0000-0003-1369-1739
M.W. Shafer 0000-0001-9808-6305
J.D. Lore 0000-0002-9192-465X
J.M. Canik 0000-0001-6934-6681
S.R. Haskey 0000-0002-9978-6597
C.J. Lasnier 0000-0002-7109-2278
A.L. Moser 0009-0005-3737-0317
T.H. Osborne 0000-0003-2641-4597
H.Q. Wang 0000-0003-1920-2799

References

[1] Snyder P.B., Groebner R.J., Hughes J.W., Osborne T.H., Beurskens M., Leonard A.W., Wilson H.R. and Xu X.Q. 2011 A first-principles predictive model of the pedestal height and width: development, testing and ITER optimization with the EPED model *Nucl. Fusion* **51** 103016

[2] Staebler G.M. *et al* 2022 Advances in prediction of tokamak experiments with theory-based models *Nucl. Fusion J.M.P.* Yong-Su Na **62** 042005

[3] Bonnin X., Dekeyser W., Pitts R., Coster D., Voskoboynikov S. and Wiesen S. 2016 Presentation of the New SOLPS-ITER code package for Tokamak Plasma edge modelling *Plasma Fusion Res.* **11** 1403102

[4] Rognlien T.D., Milovich J.L., Rensink M.E. and Porter G.D. 1992 A fully implicit, time dependent 2-D fluid code for modeling tokamak edge plasmas *J. Nucl. Mater.* **196** 347

[5] Bufferand H. *et al* 2022 Implementation of multi-component Zhdanov closure in SOLEDGE3X *Plasma Phys. Control. Fusion* **64** 055001

[6] Feng Y. *et al* 2014 Recent improvements in the EMC3-Eirene code *Contrib. Plasma Phys.* **54** 426–31

[7] Simonini R., Corrigan G., Radford G., Spence J. and Taroni A. 1994 Models and numerics in the multi-fluid 2-D edge plasma code EDGE2D/U *Contrib. Plasma Phys.* **34** 368–73

[8] Moscheni M. *et al* 2022 Cross-code comparison of the edge codes SOLPS-ITER, SOLEDGE2D and UEDGE in modelling a low-power scenario in the DTT *Nucl. Fusion* **62** 056009

[9] Horsten N. *et al* 2025 Validation of SOLPS-ITER and EDGE2D-EIRENE simulations for H, D and T JET ITER-like wall low-confinement mode plasmas *Nucl. Mater. Energy* **42** 101842
[10] Rivals N., Tamain P., Marandet Y., Bonnin X., Park J.-S., Bufferand H., Pitts R.A., Falchetto G., Yang H. and Ciraolo G. 2025 SOLEDGE3X full vessel plasma boundary simulations of ITER non-active phase plasmas *Nucl. Fusion* **65** 026038
[11] Kuang A.Q. *et al* 2020 Divertor heat flux challenge and mitigation in SPARC *J. Plasma Phys.* **86** 865860505
[12] Ballinger S.B., Kuang A.Q., Umansky M.V., Brunner D., Canik J.M., Greenwald M., Lore J.D., LaBombard B., Terry J.L. and Wigram M. 2021 Simulation of the SPARC plasma boundary with the UEDGE code *Nucl. Fusion* **61** 086014
[13] Park J.-S., Bonnin X. and Pitts R. 2021 Assessment of ITER divertor performance during early operation phases *Nucl. Fusion* **61** 016021
[14] Lore J.D., Bonnin X., Park J.-S., Pitts R.A. and Stangeby P.C. 2022 High gas throughput SOLPS-ITER simulations extending the ITER database to strong detachment *Nucl. Fusion* **62** 106017
[15] Lore J.D., Jae-Sun Park A.Q.K., Reinke M.L., De Pascuale S., Lomanowski B., Creely A.J. and Canik J.M. 2024 Evaluation of SPARC divertor conditions in H-mode operation using SOLPS-ITER *Nucl. Fusion* **64** 126054
[16] Meier E.T., Covele B., Guo H.Y. and Thomas D.M. 2018 Drift effects and up-down asymmetry in balanced double-null DIII-D divertor configurations *Contrib. Plasma Phys.* **58** 732
[17] Kawashima H., Shimizu K., Takizuka T., Asakura N., Sakurai S., Matsukawa M. and Fujita T. 2008 Design study of JT-60SA divertor for high heat and particle controllability *Fusion Eng. Des.* **83** 1643–7
[18] Osawa R.T., Moulton D., Newton S.L., Henderson S.S., Lipschultz B. and Hudoba A. 2023 SOLPS-ITER analysis of a proposed STEP double null geometry: impact of the degree of disconnection on power-sharing *Nucl. Fusion* **63** 076032
[19] Holm A. *et al* 2024 Modeling a divertor with mid-leg pumping for high-power H-mode scenarios in DIII-D considering E × B drift flows *Nucl. Mater. Energy* **41** 101782
[20] Yu J.H. *et al* 2024 Simulations of divertor designs that spatially separate power and particle exhaust using mid-leg divertor particle pumping *Nucl. Mater. Energy* **41** 101826
[21] Moser A.L., Casali L., Covele B.M., Leonard A.W., McLean A.G., Shafer M.W., Wang H.Q. and Watkins J.G. 2020 Separating divertor closure effects on divertor detachment and pedestal shape in DIII-D *Phys. Plasmas* **27** 032506
[22] Casali L., Eldon D., Boedo J.A., Leonard T. and Covele B. 2020 Neutral leakage, power dissipation and pedestal fueling in open vs closed divertors *Nucl. Fusion* **60** 076011
[23] Wensing M. *et al* (the EUROfusion MST1 Team and the TCV Team) 2019 SOLPS-ITER simulations of the TCV divertor upgrade *Plasma Phys. Control. Fusion* **61** 085029
[24] Dekeyser W. *et al* 2021 Plasma edge simulations including realistic wall geometry with SOLPS-ITER *Nucl. Mater. Energy* **27** 100999
[25] Senichenkov I., Kaveeva E., Rozhansky V., Shtyrkhunov N., Dolgova K., Ding R., Hang S. and Guoliang X. 2024 First results of EAST edge modeling with SOLPS-ITER 3.2.0 on extended grid *Contrib. Plasma Phys.* **64** e202300136
[26] d'Abusco M.S., Giorgiani G., Artaud J.F., Bufferand H., Ciraolo G., Ghendrih P., Serre E. and Tamain P. 2022 Core-edge 2D fluid modeling of full tokamak discharge with varying magnetic equilibrium: from WEST start-up to ramp-down *Nucl. Fusion* **62** 086002
[27] Sureshkumar S. *et al* 2024 First SOLEDGE3X-EIRENE simulations of the ITER Neon seeded burning plasma boundary up to the first wall *Nucl. Mater. Energy* **41** 101780
[28] Dekeyser W., Coosemans R., Carli S. and Baelmans M. 2022 A self-consistent κ-model for anomalous transport due to electrostatic, interchange-dominated E × B drift turbulence in the scrape-off layer and implementation in SOLPS-ITER *Contrib. Plasma Phys.* **62** e202100190
[29] Wiesen S. *et al* 2015 The new SOLPS-ITER code package *J. Nucl. Mater.* **463** 480
[30] Rognlien T.D. *et al* 2017 Comparison of 2D simulations of detached divertor plasmas with divertor Thomson measurements in the DIII-D tokamak *Nucl. Mater. Energy* **12** 44
[31] Lore J.D., Stangeby P.C., Guo H.Y., Covele B., Moser A. and Frerichs H. 2018 Modeling non-axisymmetry in the DIII-D small angle slot divertor using EMC3-EIRENE *Nucl. Mater. Energy* **17** 152
[32] Wiesen S. *et al* 2018 On the role of finite grid extent in SOLPS-ITER edge plasma simulations for JET H-mode discharges with metallic wall *Nucl. Mater. Energy* **17** 174–81
[33] Eich T. *et al* 2013 Scaling of the tokamak near the scrape-off layer H-mode power width and implications for ITER *Nucl. Fusion* **53** 093031
[34] Hill D.N. 1997 A review of ELMs in divertor tokamaks *J. Nucl. Mater.* **241–243** 182
[35] Maingi R., Watkins J.G., Mahdavi M.A. and Colchin R.J. 2004 Neutral pressure dynamics in the upper plenums in the DIII-D tokamak *Nucl. Fusion* **44** 909
[36] Unterberg E.A., Allen S.L., Brooks N.H., Evans T.E., Leonard A.W., McLean A., Watkins J.G. and Whyte D.G. 2011 Global particle balance measurements in DIII-D H-mode discharges *J. Nucl. Mater.* **415** S740
[37] Canik J.M., Maingi R., Soukhanovskii V.A., Bell R.E., Kugel H.W., LeBlanc B.P. and Osborne T.H. 2011 Measurements and 2-D modeling of recycling and edge transport in discharges with lithium-coated PFCs in NSTX *J. Nucl. Mater.* **415** S409
[38] Boedo J.A. *et al* 2003 Transport by intermittency in the boundary of the DIII-D tokamak *Phys. Plasmas* **10** 1670
[39] Zito A., Wischmeier M., Carralero D., Manz P., Pérez I.P. and Passoni M. 2021 Numerical modelling of an enhanced perpendicular transport regime in the scrape-off layer of ASDEX Upgrade *Plasma Phys. Control. Fusion* **63** 075003
[40] Shafer M.W. *et al* 2019 Dependence of neutral pressure on detachment in the small angle slot divertor at DIII-D *Nucl. Mater. Energy* **19** 487
[41] Horvath L. *et al* 2023 Pedestal particle balance studies in JET-ILW H-mode plasmas *Plasma Phys. Control. Fusion* **65** 044003
[42] Kaveeva E., Makarov S., Senichenkov I., Rozhansky V., Veselova I., Bonnin X. and Pitts R.A. 2023 SOLPS-ITER modeling of deuterium throughput impact on the ITER SOL plasma *Nucl. Mater. Energy* **35** 101424
[43] Maurizio R. *et al* 2021 Numerical assessment of the new V-shape small-angle slot divertor on DIII-D *Nucl. Fusion* **61** 116042
[44] Canik J.M., Briesemeister A.R., McLean A.G., Groth M., Leonard A.W., Lore J.D. and Moser A. 2017 Testing the role of molecular physics in dissipative divertor operations through helium plasmas at DIII-D *Phys. Plasmas* **24** 056116
[45] Ma X. *et al* 2025 Characterizing impurity sourcing and transport in the high temperature boundary of DIII-D wide pedestal QH-mode plasmas *Nucl. Fusion* **65** 026017
[46] Miller M.A., Hughes J.W., Mordijck S., Wigram M., Dunsmore J., Reksoatmodjo R. and Wilcox R.S. 2024

Particle control via cryopumping and its impact on the edge plasma profiles of Alcator C-Mod *Nucl. Mater. Energy* **42** 101856
[47] Miller M.A., Hughes J.W., Rosenthal A.M., Mordijck S., Reksoatmodjo R., Wigram M., Dunsmore J., Sciortino F., Wilcox R.S. and Odstrcil T. 2025 Enhanced pedestal transport driven by edge collisionality on Alcator C-Mod and its role in regulating H-mode pedestal gradients *Nucl. Fusion* **65** 026029
[48] Leonard A.W., Meyer W.H., Geer B., Behne D.M. and Hill D.N. 1995 2D tomography with bolometry in DIII-D *Rev. Sci. Instrum.* **66** 1201–4
[49] Fenstermacher M.E. *et al* 1997 The two-dimensional structure of radiative divertor plasmas in the DIII-D tokamak *Phys. Plasmas* **4** 1761
[50] Scotti F. *et al* 2023 2D characterization of radiative divertor regimes with impurity seeding in DIII-D H-mode discharges *Proc. 29th IAEA Fusion Energy Conf.*
[51] Stangeby P.C., Canik J.M., Elder J.D., Lasnier C.J., Leonard A.W., Eldon D., Makowski M.A., Osborne T.H. and Grierson B.A. 2015 Identifying the location of the OMP separatrix in DIII-D using power accounting *Nucl. Fusion* **55** 093014
[52] Leonard A.W., McLean A.G., Makowski M.A. and Stangeby P.C. 2017 Compatibility of separatrix density scaling for divertor detachment with H-mode pedestal operation in DIII-D *Nucl. Fusion* **57** 086033
[53] Pitts R.A. *et al* 2019 Physics basis for the first ITER tungsten divertor *Nucl. Mater. Energy* **20** 100696
[54] Krasheninnikov S.I. 2001 On scrape off layer plasma transport *Phys. Lett. A* **283** 368
[55] Wigram M.R.K., Ridgers C.P., Dudson B.D., Brodrick J.P. and Omotani J.T. 2020 Incorporating nonlocal parallel thermal transport in 1D ITER SOL modelling *Nucl. Fusion* **60** 076008
[56] Groebner R.J. and Osborne T.H. 1998 Scaling studies of the high mode pedestal *Phys. Plasmas* **5** 1800
[57] Emdee E.D., Horvath L., Bortolon A., Wilkie G.J., Gerrú R. and Laggner F. 2025. The influence of rotation and SOL drifts on poloidal asymmetries of pedestal fueling in preparation
[58] Maingi R., Watkins J.G., Mahdavi M.A. and Owen L.W. 1999 Pump plenum pressure dependence on divertor plasma parameters and magnetic geometry in the DIII-D tokamak *Nucl. Fusion* **39** 1187
[59] Lore J.D., Wilcox R.S., Canik J.M., Wang L., Xu G.S. and Maingi R. 2019 Optimization of pumping performance in the EAST upgraded divertor *Plasma Phys. Control. Fusion* **61** 065001
[60] Chankin A.V. *et al* 2006 SOLPS modelling of ASDEX upgrade H-mode plasma *Plasma Phys. Control. Fusion* **48** 839
[61] Ma X. *et al* 2022 E $\times$ B flow driven electron temperature bifurcation in a closed slot divertor with ion B $\times \nabla$B away from the X-point in the DIII-D tokamak *Nucl. Fusion* **62** 126048
[62] Liu X.J. *et al* 2019 Modeling study of the onset density for divertor detachment on EAST *Phys. Plasmas* **26** 102510
[63] Brunner D. *et al* 2013 An assessment of ion temperature measurements in the boundary of the Alcator C-Mod tokamak and implications for ion fluid heat flux limiters *Plasma Phys. Control. Fusion* **55** 095010
[64] Haskey S.R. *et al* 2022 Ion thermal transport in the H-mode edge transport barrier on DIII-D *Phys. Plasmas* **29** 012506
[65] Isler R.C. 1994 An overview of charge-exchange spectroscopy as a plasma diagnostic *Plasma Phys. Control. Fusion* **36** 171
[66] Haskey S.R. *et al* 2018 Active spectroscopy measurements of the deuterium temperature, rotation and density from the core to scrape off layer on the DIII-D tokamak (invited) *Rev. Sci. Instrum.* **89** 10D110
[67] Haas G. and Bosch H.-S. 1998 In vessel pressure measurement in nuclear fusion experiments with ASDEX Gauges *Vacuum* **51** 39
[68] Tsui C.K. *et al* 2022 Evidence on the effects of main-chamber neutrals on density shoulder broadening *Phys. Plasmas* **29** 062507
[69] Bernard T.N., Halpern F.D., Francisquez M., Mandell N.R., Juno J., Hammett G.W., Hakim A., Wilkie G.J. and Guterl J. 2022 Kinetic modeling of neutral transport for a continuum gyrokinetic code *Phys. Plasmas* **29** 052501